Electro-Thermo-Elastic Simulation of Graphite Tools Used in SPS Processes

Stefan Hartmann, Steffen Rothe and Nachum Frage

Abstract In the range of field-assisted sintering technology or spark plasma sintering all materials in the testing machine undergo very large temperature changes. The powder material, which has to be sintered, is filled into a graphite die and mechanically loaded by a graphite punch. The heat is produced by electrical induction and the cooling process is performed by conduction and radiation. Both the heating and the cooling process are very fast. In order to understand the process of the highly loaded graphite parts, experiments, modeling and computations have to be carried out. On the thermal side the temperature-dependent material properties such as heat capacity and heat conductivity have to be modeled. Since the heat capacity is not independent of the Helmholtz free-energy a particular consideration of the free-energy is carried out. On the other hand, the temperature changes of the electrical resistivity and the material properties of the graphite tool must be taken into considerations. Accordingly, the material properties of "Ohm's law" must be modeled as well. The fully coupled system comprising the electrical, thermal and mechanical field are solved numerically by a monolithic finite element approach. After the spatial discretization using finite elements one arrives at a system of differential-algebraic equations which is solved by means of diagonally implicit Runge-Kutta methods. Issues and open questions in the numerics are addressed and problems in modeling a real application are discussed.

S. Hartmann (✉) · S. Rothe
Institute of Applied Mechanics, Clausthal University of Technology,
Clausthal-Zellerfeld, Germany
e-mail: stefan.hartmann@tu-clausthal.de

S. Rothe
e-mail: steffen.rothe@tu-clausthal.de

N. Frage
Department of Materials Engineering, Ben-Gurion University of the Negev,
Beer-Sheva, Israel
e-mail: nfrage@bgu.ac.il

1 Introduction

The numerical treatment of powder compaction processes requires the experimental
basis, appropriate constitutive models and sophisticated algorithms both for the pow-
der and the tools itself. In field-assisted sintering technology (FAST) the mechanical
and thermal loads are applied more or less in parallel. An overview of the technical
development of FAST-processes can be found in [1–4]. In the literature there exists
only few attempts to model the whole thermo-electro-mechanical problem. In the
work of [5] the SPS-process (spark plasma sintering) is modeled without powder to
study the thermal and the electrical field together with a small strain thermoelasticity
relation for the tooling system. Wang et al. [6] investigated the electrical, tempera-
ture and stress fields in order to evaluate stress gradients in the fully densed sample
(copper and alumina). In this study the electrical current is treated as a constant.
Differently, [7] modelled the time dependence of the electrical current by the use
of experimental recorded current for a specific experiment. In [8] a PID control for
the closed loop control of the current is added to achieve a prescribed temperature
path. In this investigation temperature and stress gradients for a fully densed alumina
and copper sample are analyzed. Wang et al. [9] studied the effect of different die
sizes, heating rates and pressures on the temperature and stress distribution inside a
alumina sample, the tooling system and on the resulting microstructure. Maizza et al.
[10] investigated the influence of moving punch on the temperature. He emphasizes
the reliability of the model predictions highly depend on the correct modeling of the
contact resistances. Cincotti et al. [5] compared simulation results to measured tem-
perature, voltage and displacement data including electric and thermal resistance as
a function of temperature and applied mechanically load. Recently two articles also
dealing with the densification process are published, [11, 12]. Since the temperature
in the powder, and, accordingly the final material properties of the sintering process,
is essentially influenced by the graphite tools (given by the die, where the powder is
encapsulated, and the punches treating the mechanical loads to compress the powder),
the investigation of the die/punch system in view of the temperature and stress distri-
bution is of principle interest. Moreover, the heat is applied using electrical induction
so that the temperature and stress distribution during the processes are coupled. Since
the applied temperatures vary within a large range, most of the material parameters
depend on the temperature itself so that the final initial boundary-value problem is
a coupled system represented by the equilibrium conditions, heat equation and the
electrical field equation. In view of the investigations in [13] inertia effects are not
considered because the investigated temperature-rates are not as fast enough to take
resulting phenomena into account. Moreover, the investigated temperature are below
the phase transition effects in the graphite tools and the powder material (copper or
alumina).

   In this article we assume in the first instance thermo-elasticity for small strains and
a instationary non-linear heat equation. Particularly, small strain thermo-elasticity is
seemingly well understood, see for example, [13, 14]. However, frequently some
terms are neglected by intuition or by the assumption of small rates or small

temperature changes. These assumptions are not always applicable, particularly not in FAST-processes. In this case the graphite tools have temperature-dependent properties, such as a temperature-dependent heat-capacity, directly influencing the form of the free-energy and the thermo-mechanical coupling term. Moreover, the well-known effect of a temperature-dependent electrical resistivity influences the evolution of the electrical potential. In this article, we propose some experiments determining the temperature-dependent material properties first. These experiments are given by purely thermal agencies to determine the heat expansion, the heat capacity, the heat conductivity and the electrical resistivity. All these quantities are more or less temperature-dependent. Particularly, the heat capacity influences directly the representation of the free-energy. Thus, aspects of the modeling are touched as well. On the basis of these properties phenomenological models are developed and calibrated to the experimental data.

Since the entire problem is coupled, all practical applications have to be computed numerically. Here, use is made of the finite element method. In [15] coupled problems are discussed within the method of vertical lines. This procedure, well-known as a solution technique for partial differential equations, makes use of two subsequent steps, namely the spatial and the temporal discretization. In our case the spatial discretization using finite elements yields a system of differential-algebraic equations, or, shortly, a DAE-system. In other words, ordinary differential equations are coupled with algebraic equations. In this context, the differential part of the DAE-system results from the discretized instationary non-linear heat equation and the algebraic parts stem from the discretized equilibrium equations and the stationary charge equation, see for general remarks [16]. These systems are frequently solved using a Backward-Euler scheme or a trapezoidal rule (Crank-Nicholson procedure) for the differential part resulting from the fact that the numerical solution of DAEs are commonly not known in the finite element literature. In this article, high-order stiffly accurate diagonally-implicit Runge-Kutta methods (SDIRK-methods), see, for example, [17, 18], are applied having the side-product of an efficient step-size control technique. The reason for this stems from the application of embedded SDIRK methods.

The notation in use is defined in the following manner: geometrical vectors are symbolized by lower case bold-faced letters $\mathbf{a}$ and second order tensors $\mathbf{A}$ by bold-faced Roman letters. Furthermore, we introduce matrices at global level of the finite element procedure symbolized by bold-faced italic letters $\boldsymbol{A}$.

2 Constitutive Modeling and Initial Boundary-Value Problem

Before developing a constitutive model for the graphite material, the mechanical, thermal and electrical properties are discussed. The elasticity parameters are determined using ultrasound measurements, [19, 20], leading to the Young's modulus $E = 11500 \text{ N/mm}^2$ and the Poisson-ratio $\nu = 0.2$. The temperature-dependence of the elasticity parameters cannot be provided. Moreover, any viscous effects or

remaining deformations are, currently, not known, i.e. measured. Thus, a model of linear thermo-elasticity is assumed. Moreover, any viscous effects or remaining deformations are not taken into considerations. Thus, a model of thermo-elasticity is assumed. The heat expansion is measured to be nearly temperature-independent within the measured range of temperature, see Fig. 1a. According to the assumption that the thermal strains are purely volumetrical,

$$\mathbf{E}_\Theta = \varphi(\Theta(\mathbf{x}, t))\mathbf{I} \tag{1}$$

(pure volumetric heat expansion), Fig. 1a suggest the linear function

$$\varphi(\Theta) = \alpha_\Theta \vartheta = \alpha_\Theta(\Theta - \Theta_0), \tag{2}$$

where α_Θ is the heat expansion coefficient, $\vartheta(\mathbf{x}, t) = \Theta(\mathbf{x}, t) - \Theta_0$ the temperature difference, Θ_0 the reference temperature, and Θ the absolute temperature. The heat expansion coefficient is given by $\alpha_\Theta = 4.55 \times 10^{-6}$ 1/K (here, use is made of a Unitherm 1252 ultra high temperature dilatometer). Further measurements are carried out using a Netzsch Laserflash-device LFA 457 to determine the temperature-dependent heat conductivity, see Fig. 2a. The heat capacity at constant pressure is provided by the manufacturer of the material and the mathematical representation is shown in Fig. 2b.

In order to obtain a more or less reasonable curvature, even outside the range of experimental data, the functions

$$\kappa_\Theta(\Theta) = b_1 e^{-b_2\Theta} + b_3 e^{-b_4\Theta} \tag{3}$$
$$c_\Theta(\Theta) = d_1 + d_2\Theta + d_3 \tanh(d_4\Theta - d_5) \tag{4}$$
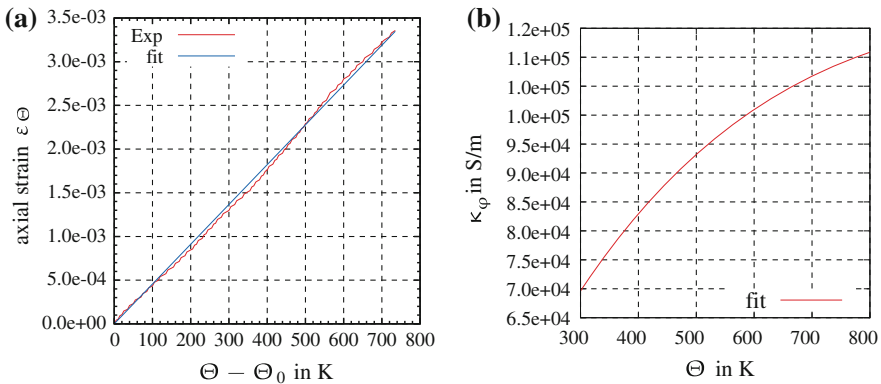
are chosen. The parameters are identified with

Fig. 1 Heat expansion and electrical conductivity in dependence of the temperature of graphite. (**a**) Heat expansion, (**b**) Electrical conductivity
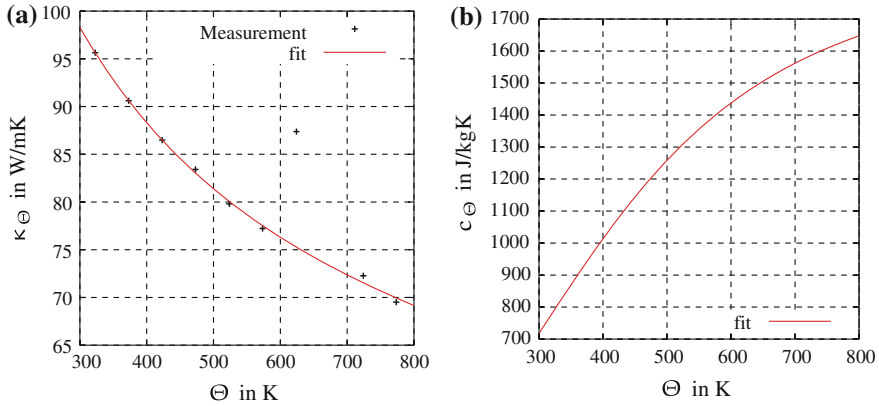
Fig. 2 Heat conductivity and heat capacity in dependence of the temperature. (**a**) Heat conductivity, (**b**) Heat capacity

$$b_1 = 85.7 \, \frac{W}{mK}, b_2 = 5.124 \times 10^{-3} \, \frac{1}{K}, b_3 = 88.1 \, \frac{W}{mK}, b_4 = 3.292 \times 10^{-4} \, \frac{1}{K},$$

$$d_1 = 586.5 \, \frac{J}{kgK}, d_2 = 0.3507 \, \frac{J}{kgK^2}, d_3 = 839.4 \, \frac{J}{kgK}, d_4 = 3.247 \times 10^{-3} \, \frac{1}{K},$$

and $d_5 = 0.9431$.

In Fig. 1b the model response of the data for the electrical conductivity in dependence of the temperature provided by the manufacturer is shown as well, which is modeled by

$$\kappa_\varphi(\Theta) = c_1 e^{-c_2\Theta} - c_3 e^{-c_4\Theta} \tag{5}$$

with

$$c_1 = 1.69 \times 10^5 \, \frac{S}{m}, c_2 = 2.168 \times 10^{-4} \, \frac{1}{K}, c_3 = 1.661 \times 10^5 \, \frac{S}{m}, c_4 = 2.089 \times 10^{-3} \, \frac{1}{K}.$$

The mechanical constitutive equations are applied as follows. First of all, a dependence of the mechanical material parameters on the electrical current and the temperature is not assumed. These properties have not been available so far. For a first instance thermo-elasticity is assumed. There, it is common to prescribe a specific free-energy function and calculate the heat capacity, or to define the heat capacity constant (commonly contradicting the choice of the specific free-energy), or to make use of the experimentally determined heat capacity and to integrate those equations to obtain the specific free-energy. Here, use is made of the latter concept. Thus, the case of thermo-elasticity has to be recapped. Since we assume small strains, the linearized strain tensor $\mathbf{E}(\mathbf{x}, t) = (\text{grad } \mathbf{u}(\mathbf{x}, t) + \text{grad }^T\mathbf{u}(\mathbf{x}, t))/2$ is introduced. $\mathbf{u}(\mathbf{x}, t)$ defines the displacement field, where $\mathbf{x}$ symbolizes the spatial coordinate and t defines the time. As it is common, the strain tensor is decomposed into a mechanical $\mathbf{E}_M$ and a

thermal part $\mathbf{E}_\Theta$,

$$\mathbf{E} = \mathbf{E}_M + \mathbf{E}_\Theta, \tag{6}$$

with $\mathbf{E}_\Theta$ given in Eq. (1). In view of the subsequent development the strain-rates are required, i.e. the mechanical strain-rate reads

$$\dot{\mathbf{E}}_M = \dot{\mathbf{E}} - \dot{\mathbf{E}}_\Theta = \dot{\mathbf{E}} - \alpha_\Theta \dot{\Theta} \mathbf{I} \quad \text{with} \quad \dot{\mathbf{E}}_\Theta = \alpha_\Theta \dot{\Theta} \mathbf{I}. \tag{7}$$

In the following, it is assumed that the free-energy $\psi(\mathbf{E}_M, \Theta)$ can be decomposed into one part $\psi_M(\mathbf{E}_M)$ depending only on the mechanical-based deformation, and another part $\psi_\Theta(\Theta)$ resulting from the temperature effects

$$\psi(\mathbf{E}_M, \Theta) = \psi_M(\mathbf{E}_M) + \psi_\Theta(\Theta). \tag{8}$$

In the case of linear thermo-elasticity

$$\rho \psi_M(\mathbf{E}_M) = \frac{K}{2} (\operatorname{tr} \mathbf{E}_M)^2 + G \mathbf{E}_M^D \cdot \mathbf{E}_M^D \tag{9}$$

defining the mechanical part of the specific free-energy (isotropic linear elasticity relation), where K symbolizes the bulk modulus, G the shear modulus, and $\rho(\mathbf{x})$ the mass density. For the given Young's modulus E and the Poisson-ratio ν the bulk and shear moduli are

$$K = \frac{E}{3(1-2\nu)} = 6389 \text{N/mm}^2, \quad G = \frac{E/}{2(1+\nu)} = 4792 \text{N/mm}^2,$$

respectively.

Remark 8.1. The elastic constants might be depend on the temperature. However, the experimental results for the underlying material are still an open issue. Accordingly, as a first attempt temperature-independent bulk and shear moduli are assumed. This also addresses the form of the classically simple form of the specific free-energy function. □

$\operatorname{tr} \mathbf{A} = a_k^k$ defines the trace and $\mathbf{A}^D = \mathbf{A} - 1/3(\operatorname{tr} \mathbf{A})\mathbf{I}$ denotes the deviator operator of a second order tensor $\mathbf{A}$. $\operatorname{tr} \mathbf{E}_M$ is interpreted as the volumetric mechanical strains resulting from the interpretation that for the isothermal, small strain theory $\varepsilon_V := \operatorname{tr} \mathbf{E} = \operatorname{tr}(\operatorname{grad} \mathbf{u}) = \operatorname{div} \mathbf{u}$ holds, where ε_V represents the volumetric strain. The thermal part of the free-energy is unknown so far and is related to the heat capacity.

The Clausius-Duhem inequality (CDI) is assumed to guarantee thermo-mechanical consistence, which reads

$$-\dot{e} + \Theta \dot{s} + \frac{1}{\rho} \mathbf{T} \cdot \dot{\mathbf{E}} - \frac{1}{\Theta} \mathbf{q} \cdot \mathbf{g} \geqslant 0. \tag{10}$$

$e(\mathbf{x}, t)$ is the specific internal energy, $s(\mathbf{x}, t)$ the specific entropy, $\mathbf{q}(\mathbf{x}, t)$ the heat flux vector, and $\mathbf{g}(\mathbf{x}, t) = \operatorname{grad} \Theta(\mathbf{x}, t)$ the temperature gradient, see [21]. Additionally, it is assumed that there exists a relation between the specific internal energy e and the free-energy ψ, the total temperature Θ and the specific entropy s by

$$e = \psi + \Theta s \tag{11}$$

implying

$$\dot{e} = \dot{\psi} + \dot{\Theta}s + \Theta\dot{s}. \tag{12}$$

Inserting this relation and the time-derivative of the free-energy

$$\dot{\psi} = \frac{\partial\psi}{\partial\mathbf{E}_M} \cdot \dot{\mathbf{E}}_M + \frac{\partial\psi}{\partial\Theta}\dot{\Theta} = \frac{d\psi_M}{d\mathbf{E}_M} \cdot \dot{\mathbf{E}}_M + \frac{d\psi_\Theta}{d\Theta}\dot{\Theta} \tag{13}$$

into the CDI (10) yields the inequality

$$-\dot{\psi} - \dot{\Theta}s + \frac{1}{\rho}\mathbf{T}\cdot\dot{\mathbf{E}} - \frac{1}{\Theta}\mathbf{q}\cdot\mathbf{g} \geqslant 0 \tag{14}$$

i.e.

$$-\frac{d\psi_M}{d\mathbf{E}_M} \cdot \dot{\mathbf{E}}_M - \frac{d\psi_\Theta}{d\Theta}\dot{\Theta} - s\dot{\Theta} + \frac{1}{\rho}\mathbf{T}\cdot(\dot{\mathbf{E}}_M + \dot{\mathbf{E}}_\Theta) - \frac{1}{\Theta}\mathbf{q}\cdot\mathbf{g} =$$

$$= \left(\frac{1}{\rho}\mathbf{T} - \frac{d\psi_M}{d\mathbf{E}_M}\right) \cdot \dot{\mathbf{E}}_M - \left(s + \frac{d\psi_\Theta}{d\Theta} - \frac{\alpha_\Theta}{\rho}\mathbf{T}\cdot\mathbf{I}\right) \cdot \dot{\Theta} - \frac{1}{\Theta}\mathbf{q}\cdot\mathbf{g} \geqslant 0, \tag{15}$$

where in addition to Eq. $(7)_2$ the decomposition $(7)_1$ is taken into consideration. Using $\operatorname{tr}\mathbf{T} = \mathbf{T}\cdot\mathbf{I}$, the strain-energies (9) and $\psi_\Theta(\Theta)$ yield for arbitrary processes the classical potential relations for the assumption of a small strain thermo-elastic material

$$\mathbf{T} = \rho\frac{d\psi_M}{d\mathbf{E}_M} = K(\operatorname{tr}\mathbf{E}_M)\mathbf{I} + 2G\mathbf{E}_M^D = K(\operatorname{tr}\mathbf{E} - 3\alpha_\Theta\vartheta)\mathbf{I} + 2G\mathbf{E}^D \tag{16}$$

$$s = -\frac{d\psi_\Theta}{d\Theta} + \frac{\alpha_\Theta}{\rho}(\operatorname{tr}\mathbf{T}) = -\frac{d\psi_\Theta}{d\Theta} + \frac{3\alpha_\Theta K}{\rho}(\operatorname{tr}\mathbf{E} - 3\alpha_\Theta\vartheta) \tag{17}$$

Furthermore, $(1/\Theta)\mathbf{q}\cdot\mathbf{g} \leqslant 0$ has to be satisfied, which, frequently, is modeled by Fourier's model

$$\mathbf{q} = -\kappa_\Theta(\Theta)\mathbf{g} = -\kappa_\Theta(\Theta)\operatorname{grad}\Theta, \tag{18}$$

where $\kappa_\Theta(\Theta) \geqslant 0$ represents the temperature-dependent heat conductivity. Thus, all constitutive assumptions are explained, only the thermal part of the specific free-

energy function, $\psi_\Theta(\Theta)$, is unknown so far and has to be determined by the heat capacity c_Θ.

In the following, the coupled partial differential equations required for computing boundary-value problems must be derived. First of all, the elasticity relation (16) has to be inserted into the balance of linear momentum (here the inertia terms are neglected)

$$\text{div }\mathbf{T} + \rho\mathbf{k} = \mathbf{0}, \tag{19}$$

where $\rho\mathbf{k}$ is the specific volume force ($\mathbf{k}$ represents the acceleration of gravity). Second, the balance of energy must be considered

$$\dot{e} = -\frac{1}{\rho}\text{div }\mathbf{q} + r_\varphi + p. \tag{20}$$

p defines the stress power describing the coupling term

$$p = \frac{1}{\rho}\mathbf{T}\cdot\dot{\mathbf{E}} = \frac{d\psi_M}{d\mathbf{E}_M}\cdot\dot{\mathbf{E}} = (K(\text{tr }\mathbf{E} - 3\alpha_\Theta\vartheta)\mathbf{I} + 2G\mathbf{E}^D)\cdot\dot{\mathbf{E}}, \tag{21}$$

i.e. it represents a heat source for the heat equation resulting from the mechanical behavior. r_φ symbolizes a volumetrically distributed heat source caused by the electrical current, see Eq. (30).

It is common, to exchange the internal energy e in the instationary non-linear heat equation (20) by the rate of the specific internal energy (12). Using Eqs. (7), (13), (16) and (17) leads to

$$\rho\dot{\psi} = \rho\frac{d\psi_M}{d\mathbf{E}_M}\cdot(\dot{\mathbf{E}} - \alpha_\Theta\dot{\Theta}\mathbf{I}) + \rho\frac{d\psi_\Theta}{d\Theta}\dot{\Theta} = \mathbf{T}\cdot\dot{\mathbf{E}} - \rho\left(\alpha_\Theta(\text{tr }\mathbf{T}) - \frac{d\psi_\Theta}{d\Theta}\right)\dot{\Theta}$$
$$= \mathbf{T}\cdot\dot{\mathbf{E}} - \rho s\dot{\Theta}. \tag{22}$$

It follows that the instationary non-linear heat equation, see Eqs. (20) and (12), reads

$$\rho\Theta\dot{s} = -\text{div }\mathbf{q} + \rho r_\varphi. \tag{23}$$

The time-derivative of the specific entropy s in Eq. (17),

$$\dot{s} = \left(\frac{9K\alpha_\Theta^2}{\rho} + \frac{d^2\psi_\Theta}{d\Theta^2}\right)\dot{\Theta} + \frac{3\alpha_\Theta K}{\rho}(\text{tr }\dot{\mathbf{E}}), \tag{24}$$

can be inserted now,

$$\rho\left(-\frac{d^2\psi_\Theta}{d\Theta^2} - \frac{9K\alpha_\Theta^2}{\rho}\right)\Theta\dot{\Theta} = \text{div}\,(\kappa_\Theta(\Theta)\,\text{grad}\,\Theta) + \rho r_\varphi - 3\alpha_\Theta K(\text{tr }\dot{\mathbf{E}})\Theta. \tag{25}$$

This is the analytically exact form of the instationary heat equation in thermo-elasticity without any further assumptions to reduce its complexity. The mathematical structure is as follows

$$\rho c_\Theta(\Theta)\dot{\Theta} = \text{div}\left(\kappa_\Theta(\Theta)\,\text{grad}\,\Theta\right) + \rho r_\varphi - \gamma(\dot{\mathbf{E}}, \Theta) \tag{26}$$

which is coupled with the local balance equation (19) and the elasticity relation (16). Obviously, the typical assumption of a constant specific heat capacity

$$c_\Theta(\Theta) = -\left(\frac{d^2\psi_\Theta}{d\Theta^2} - \frac{9K\alpha_\Theta^2}{\rho}\right)\Theta \tag{27}$$

is not valid anymore, see Fig. 2b, and it occurs a thermo-elastic coupling (production) term

$$\gamma(\dot{\mathbf{E}}, \Theta) = 3\alpha_\Theta K\Theta(\text{tr}\,\dot{\mathbf{E}}), \tag{28}$$

which is commonly not considered due to the fact that it is very small. In view of the heat capacity (4) the thermal part of the specific free-energy in Eq. (27) one obtains

$$\frac{d^2\psi_\Theta}{d\Theta^2} = -\frac{1}{\Theta}d_1 - d_2 - \frac{d_3}{\Theta}\tanh(d_4\Theta - d_5) + \frac{9K\alpha_\Theta^2}{\rho}. \tag{29}$$

However, the second term is analytically non-integrable. Of course, it is possible to generate a power series around Θ_0, but this is not the scope of the article and is not necessary within the whole approach. It must be remarked that for a temperature-dependent heat expansion or more sophisticated constitutive models it is hard to obtain a consistent relation between the specific free-energy and the heat capacity. Another possibility is to assume a free energy $\psi_\Theta(\Theta)$ reflecting the experimental data. The advantage is that one has only to carry out two differentiation steps. However, one has to know a priorily the course of the curve of the second derivative $\psi_\Theta''(\Theta)$, which does not simplify the problem. In the case of small strain thermo-elasticity the proposed approach has no influence although there is no analytical expression. However, for models of internal variables or in the case of large strains there is a discrepancy, which commonly is overcomed by assuming $\psi_\Theta(\Theta)$ and letting c_Θ constant being a rough approximation. In the case of large temperature changes, however, this is a very rough assumption. The remaining coupling term results from the heat generation by the electrical current, which is described by the volumetrical heat source r_φ, called Joule-heating, in Eq. (26),

$$r_\varphi = \frac{1}{\rho}\mathbf{e}\cdot\mathbf{j} = \frac{1}{\rho}\kappa_\varphi(\Theta)\text{grad}\,\varphi(\mathbf{x}, t)\cdot\text{grad}\,\varphi(\mathbf{x}, t), \tag{30}$$

where the electrical field $\mathbf{e}(\mathbf{x}, t) = -\text{grad}\,\varphi(\mathbf{x}, t)$ is related to the electrical potential $\varphi(\mathbf{x}, t)$ and the electrical current $\mathbf{j}(\mathbf{x}, t) = \kappa_\varphi(\Theta)\mathbf{e}(\mathbf{x}, t)$ reflects Ohm's law.

$\kappa_\varphi(\Theta)$, see Eq. (5), defines the electrical conductivity. In other words, there is a coupling between the electrical potential $\varphi(\mathbf{x}, t)$ in electrostatics and the conservation of charge

$$\operatorname{div} \mathbf{j}(\mathbf{x}, t) = 0, \quad \text{i.e.} \quad \operatorname{div}(\kappa_\varphi(\Theta)\operatorname{grad} \varphi) = 0, \tag{31}$$

(assumption of a stationary electrical current, see [16, 22, 23] for further reading as well). In conclusion, there is a coupling of the three partial differential equations (19), (26) and (31). The non-linearities result from the temperature-dependence of the material parameters and the boundary-conditions such as convection and radiation.

3 Time-Adaptive Monolithic Finite Element Approach

In the following, the coupled equations mentioned above, i.e. the equilibrium conditions (19), with the thermo-elasticity relation (16), the instationary non-linear heat equation (25), i.e. (26), using the abbreviations (27), (28) and (30), and the stationary current equation (31), are treated within finite elements. Here, use is made of the method of vertical lines, where in the first step the spatial discretization is carried out using the finite element discretization, see [15]. In the second step the temporal discretization is performed applying stiffly accurate diagonally implicit Runge-Kutta methods.

The weak formulation of Eq. (19) is derived by multiplying the partial differential equation with virtual displacements, integrating over the volume and applying the divergence theorem

$$\int_V \mathbf{T} \cdot \delta \mathbf{E} \, dV - \int_A \mathbf{t} \cdot \delta \mathbf{u} \, dA - \int_V \rho \mathbf{k} \cdot \delta \mathbf{u} \, dV = 0, \tag{32}$$

where $\delta \mathbf{E}(\mathbf{x}) = (\operatorname{grad} \delta \mathbf{u}(\mathbf{x}) + \operatorname{grad}^\mathsf{T} \delta \mathbf{u}(\mathbf{x}))/2$ defines the virtual strain tensor, i.e. the symmetric part of the gradient of the virtual displacements $\delta \mathbf{u}(\mathbf{x})$. In this context it has to hold $\delta \mathbf{u}(\mathbf{x}) = \mathbf{0}$ on the boundary $A^\mathbf{u}$ of the material body, where the displacements are prescribed, $A = A^\sigma \cup A^\mathbf{u}$, $\mathbf{u}(\mathbf{x}, t) = \mathbf{q}u(t)$ on $A^\mathbf{u}$ (Dirichlet boundary conditions). $\mathbf{t}(\mathbf{x}, t) = \mathbf{T}(\mathbf{x}, t)\mathbf{n}(\mathbf{x}, t)$ defines the stress vector on the surface A^σ, where $\mathbf{n}$ represents the surface normal. $\mathbf{t}(\mathbf{x}, t) = \mathbf{q}t(\mathbf{x}, t)$ on A^σ define the Neumann boundary conditions. V stands for the volume of the material body.

In the case of the instationary non-linear heat equation (26) the derivation is similar. First, the heat equation is multiplied with the virtual temperatures $\delta \Theta(\mathbf{x})$, integrated over the volume, and the divergence theorem is applied,

$$\int_V \rho c_\Theta(\Theta)\dot{\Theta}\delta\Theta \, dV = \int_A q \, \delta\Theta \, dA - \int_V \kappa_\Theta(\Theta)\operatorname{grad} \Theta \cdot \operatorname{grad} \delta\Theta \, dV$$
$$+ \int_V (\rho r_\varphi - \gamma(\dot{\mathbf{E}}, \Theta))\delta\Theta \, dV, \tag{33}$$

see [24–26]. Analogously to the mechanical field problem, the virtual temperature has the property $\delta\Theta = 0$ on A^{Θ}, i.e. the surface where the temperatures are known, $\Theta(\mathbf{x}, t) = \overline{\Theta}(\mathbf{x}, t)$ on A^{Θ} (Dirichlet boundary conditions). Furthermore, on the boundary A^q the heat transport $q = -\mathbf{q} \cdot \mathbf{n}$ is prescribed, $q(\mathbf{x}, t) = \overline{q}(\mathbf{x}, t)$ on A^q, $A = A^{\Theta} \cup A^q$. In the case of convection the linear model $q(\Theta) = h(\Theta - \Theta_{\text{ref}})$ and for radiation the non-linear boundary condition $q(\Theta) = \sigma\varepsilon(\Theta^4 - \Theta_{\infty}^4)$ are considered, where σ symbolizes the Stefan Boltzmann constant and ε the emissivity.

The equation of electrostatics (31) can be treated similar to the heat equation because it has the same mathematical structure. In this context one obtains

$$\int_V \kappa_{\varphi}(\Theta)\text{grad } \varphi \cdot \text{grad } \delta\varphi \, dV = \int_A j \, \delta\varphi \, dA \tag{34}$$

where $\delta\varphi$ represents the virtual electrical potential and j the electrical current density. Analogously, $\delta\varphi = 0$ on A^{φ}, i.e. the surface where the electrical potential is prescribed, $\varphi(\mathbf{x}, t) = \overline{\varphi}(\mathbf{x}, t)$ on A^{φ} (Dirichlet boundary conditions). Furthermore, on the boundary A^J the electrical current density $j = -\mathbf{j} \cdot \mathbf{n}$ is prescribed, $j(\mathbf{x}, t) = \overline{j}(\mathbf{x}, t)$ on A^J, $A = A^{\varphi} \cup A^J$.

The equation of electrostatics to compute thermoelectric coupling effects can be found in several publications. In Seifert et al. [27] a one dimensional model is solved by Mathematica to compute the thermoelectric behavior of Peltier coolers. In the work of Pérez-Aparicio et al. [28] a three-dimensional, non-linear fully coupled thermoelectric finite element simulation is carried out in order to simulate Peltier coolers. They included the Seebeck, Peltier, Thompson, and Joule effect in their analysis. The finite element method is combined with a Monte Carlo simulation for a material sensitivity analysis. Palma et al. [29] used a modified Fourier law yielding a hyperbolic heat equation for the simulation of micro-devices under rapid transient effects. They simulated thermoelectric material with a non-linear dynamic finite element formulation. Munir et al. [30] simulated the current and temperature distributions to find out temperature and current gradients in axial and radial direction for a SPS-process. In the underlying article, however, the field is coupled to mechanical and thermal influences.

The spatial discretization makes use of shape functions for the displacements, the temperature and the electrical potential. This leads to the linear system of equations (in two unknowns)

$$\mathbf{K}_{\text{u}}\mathbf{u}(t) + \mathbf{K}_{\text{u}\Theta}\mathbf{\Theta}(t) = \mathbf{r}_{\text{u}}(t), \tag{35}$$

where $\mathbf{u}(t) \in \mathbb{R}^{n_{\text{u}}}$ are the unknown nodal displacements and $\mathbf{\Theta}(t) \in \mathbb{R}^{n_{\Theta}}$ the unknown nodal temperatures. $\mathbf{K}_{\text{u}}$ symbolizes the mechanical stiffness matrix of linear elasticity and $\mathbf{K}_{\text{u}\Theta}$ the stiffness matrix resulting from the heat expansion. The right-hand side contains the prescribed Dirichlet- and Neumann boundary conditions and a term coming from the reference temperature Θ_0. The weak form of the heat equation (33) can be treated in a similar manner, see, for example, [25], yielding the system of ordinary differential equations

Table 1 Material parameters of the materials in a FAST-process

Material	c_Θ	κ_Θ	κ_φ	α_Θ	ρ	E	ν
	$mm^2/(s^2K)$	$tmm/(s^3K)$	$10^{-3}A/(Vmm)$	$1/K$	t/mm^3	MPa	–
Copper	$c_{\Theta,Cu}(\Theta)$	$\kappa_{\Theta,Cu}(\Theta)$	$\kappa_{\varphi,Cu}(\Theta)$	1.6×10^{-5}	8.92×10^{-9}	120 000	0.3
Alumina	$c_{\Theta,Al}(\Theta)$	$\kappa_{\Theta,Al}(\Theta)$	1×10^{-8}	8.5×10^{-6}	3.7×10^{-9}	350 000	0.22
(Al_2O_3)							
Graphite	$c_\Theta(\Theta)$	$\kappa_\Theta(\Theta)$	$\kappa_\varphi(\Theta)$	4.55×10^{-6}	1.85×10^{-9}	11500	0.2

The material functions $\kappa_\Theta(\Theta)$, $\kappa_\varphi(\Theta)$, and $c_\Theta(\Theta)$ are given in Eqs. (3), (4) and (5)

$$\boldsymbol{C}_\Theta(t,\boldsymbol{\Theta})\dot{\boldsymbol{\Theta}}(t) = \boldsymbol{r}_\Theta(t,\dot{\boldsymbol{u}},\boldsymbol{\Theta},\boldsymbol{\Phi}). \tag{36}$$

$\boldsymbol{C}_\Theta \in \mathbb{R}^{n_\Theta \times n_\Theta}$ represents the temperature-dependent heat capacity matrix and $\boldsymbol{r}_\Theta \in \mathbb{R}^{n_\Theta}$ contains the right-hand side of Eq. (33), i.e. the heat conduction and the terms resulting from the boundary conditions and the heat source of the electrical potential. The coupling results from Joule heating, i.e. it depends on the nodal values of the electrical potential $\boldsymbol{\Phi}(t)$. Analogously, the charge equation (34) leads in its discretized form to

$$\boldsymbol{K}_\varphi(t,\boldsymbol{\Theta})\boldsymbol{\Phi}(t) = \boldsymbol{r}_\varphi(t,\boldsymbol{\Theta}), \tag{37}$$

where the "stiffness matrix" $\boldsymbol{K}_\varphi \in \mathbb{R}^{n_\varphi \times n_\varphi}$ is temperature-dependent caused by the electrical conductivity. $\boldsymbol{\Phi}(t) \in \mathbb{R}^{n_\varphi}$ are the unknown nodal values of the electrical potential. Equations (35), (36) and (37) represent a DAE-system, where the algebraic part results from the mechanical equilibrium conditions (35) and the equation of electrostatics (37) and the differential part stems from the instationary heat equation (36). According to a number of publications use is made of stiffly accurate diagonally implicit Runge-Kutta methods (SDIRK-methods) having the advantage to be of higher order and to have time-adaptivity for free by a local error estimation using embedded schemes, see for their basic ideas [17, 18, 31], in the context of constitutive modeling with evolutionary-type [32–35] and for further problems [25, 36, 37]. The application of SDIRK-methods yields in each stage (points in time in the interval t_n to t_{n+1}) a coupled system of non-linear equations, which can be solved by any kind of non-linear equation solver. In the examples below the Newton-Raphson and the Newton-Raphson-Chord method are applied, see [38, 39].

4 Simulations

In the following the application of SDIRK-methods is investigated. Here, a real process occurring in field assisted sintering is studied and the problems concerned are worked out. For these computations the material parameters are compiled in Table 1. The material functions for copper and alumina are listed in the appendix.
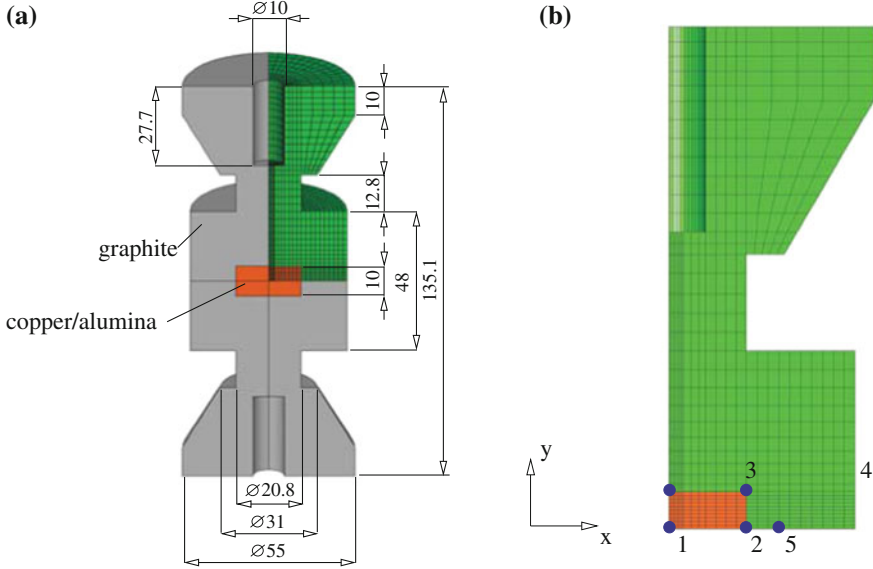
Fig. 3 Mesh (linear hexahedral elements with $n_u = 27722$, $n_\Theta = 9907$, and $n_\varphi = 9588$ unknowns) and geometry. **a** Geometry in mm, **b** Mesh and evaluation points in xy-plane
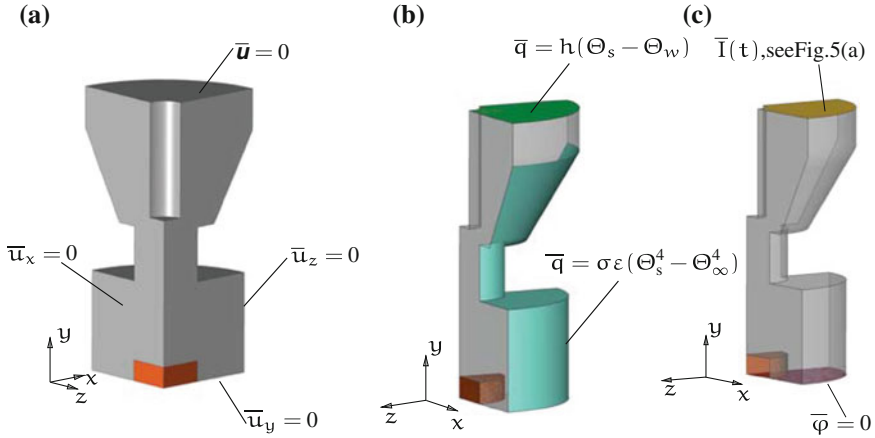

Fig. 4 Boundary conditions. **a** Mechanical field, **b** Thermal field, **c** Electrical field

In Fig. 3 the geometry of a die/punch system is shown, where the rectangular region close to the center contains the compacted powder material. In this context it has to be mentioned that not the compaction process itself is treated, but "only" the temperature evolution in the die/punch/powder system is studied. The boundary conditions are shown in Fig. 4 for the displacements/forces, temperatures/heat fluxes, and electrical potential/electrical current at the surfaces. Θ_s is the surface temperature
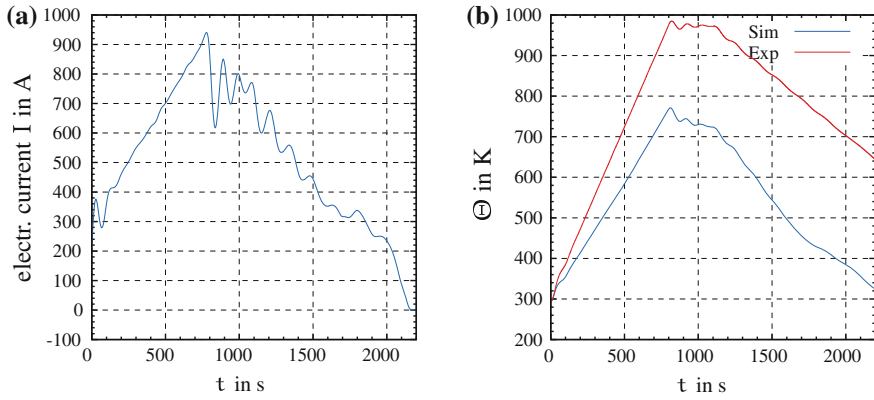
Fig. 5 Measured electrical current taken from the FAST-machine used as boundary condition. **a** Prescribed electrical current ($I = \int_A \mathbf{j} \cdot \mathbf{n} \, dA$), **b** Measured and simulated temperature evolution in point 5 ($\Theta_0 = 273$ K)

of the graphite tools, Θ_w the water temperature and h the heat transfer coefficient ($h = 0.88 \, t/(s^3 K), \Theta_w = 295.15K$). This represents a very rough modeling of the cooling channels in the steel parts adjacent to the upper graphite surface. In view of radiation the classical model is chosen having the Boltzmann constant $\sigma = 5.6704 \times 10^{-12} t/(s^3 K^4)$ and the emissivity of $\varepsilon = 0.8$. The temperature of the chamber wall is supposed to be $\Theta_\infty = 303.15$ K. Since the chamber is under vacuum, convection on the lateral surfaces is not taken into consideration.

From the testing machine one obtains the data of the electrical current prescribed at the upper surface, see Fig. 5a for the smoothed response. In Fig. 5b the temperature response for copper powder is depicted, see for the chosen material [40], showing that the temperature at point 5 is underestimated, see Fig. 3. The heating rate in the experiment is $\dot{\Theta} = 50$ K/min. The reason of this can be seen for the absence of heat reflection in the machine's chamber, which leads to a larger surface temperature, and the inaccurate modeling of the convection at the upper surface, where the adjacent steel parts with the water cooling channels are located. However, more pronounced seems to be the influence of the electrical contact conditions between steel and graphite, graphite-graphite and graphite-powder, as reported in [10, 41, 42], which is not modeled. Particularly, an imperfect contact changes the resistivity and, accordingly, the heat generation. First attempts using a commercial finite element program confirms this behavior, which is not shown here.

The comparison of electrically conducting and non-conducting material (copper powder and a ceramic powder (alumina)) yields the fact that the electrically insulating powder increases the heat in the graphite tool, see Fig. 6a, which is obvious since the electrically conducting cross-section is smaller for ceramic powder than for metal powder. However, the temperature inside the die is homogenously distributed as indicated in Fig. 6b.
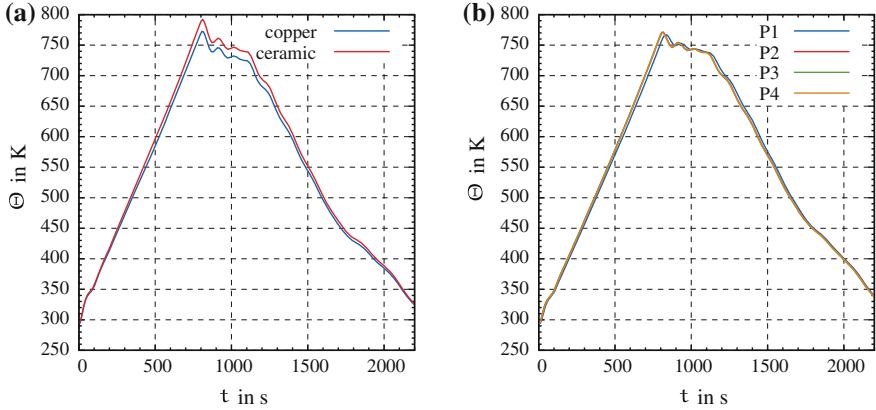
Fig. 6 Comparison of electrical conducting and non-conducting copper and ceramic powder. **a** Comparison between copper and ceramic powder in point 1, **b** Temperature for ceramic powder at the four corners 1–4, see numbering in Fig. 3b
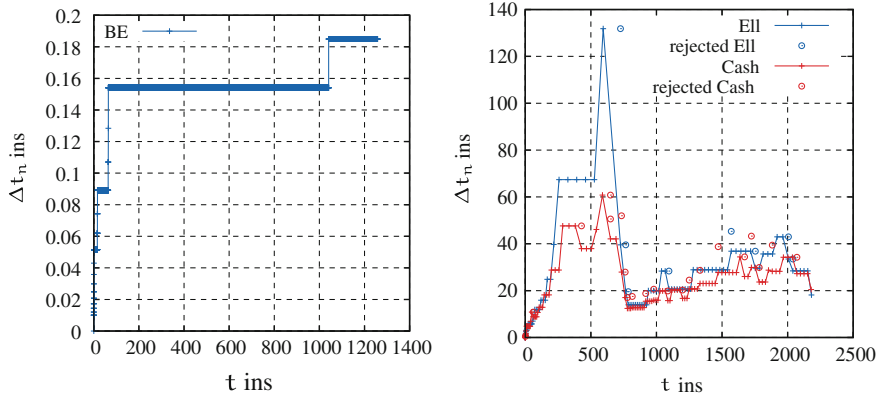

Fig. 7 Step-size behavior using various time-integrator. **a** Backward-Euler method with step-size control using the number of iterations, **b** Method of Ellsiepen (2nd order) and Cash (3rd order) using embedded methods

In view of the numerical treatment using time-adaptive SDIRK-methods, the classical Backward-Euler scheme is chosen as a first choice. Using this procedure a common adaptive scheme makes use of the number of Newton-Raphson iterations to estimate the step-size. If the number of iterations is less than 5, the step-size is increased. However, if one looks at the step-size behavior in Fig. 7a, an appropriate computational time cannot be obtained (we terminated the computation due to an excessive computational amount). Thus, a time-adaptive second-order and third-order SDIRK-method of Ellsiepen, see [32, 43], and [44], are applied leading to much larger time increments. Accordingly, reasonable computational costs are obtained. However, there are a number of step-size rejections resulting from
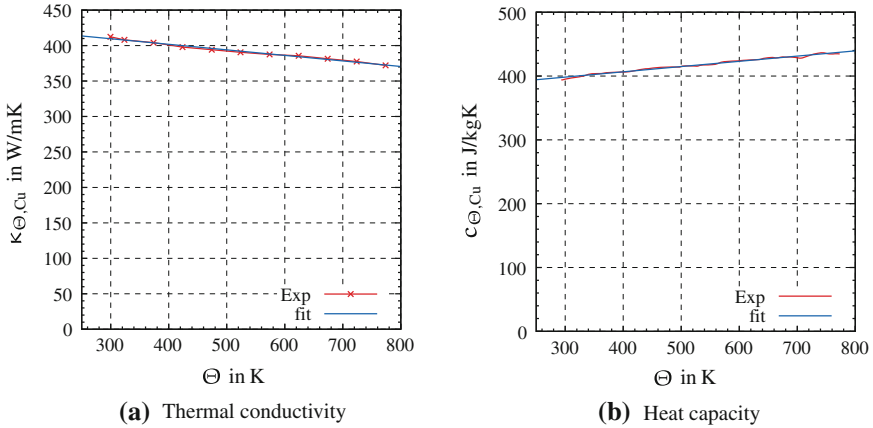
(a) Thermal conductivity   **(b)** Heat capacity

Fig. 8 Heat conductivity and heat capacity of copper in dependence of the temperature. **a** Thermal conductivity, **b** Heat capacity

the non-smoothness of the prescribed electrical current function. It seems that the second-order method of Ellsiepen is better than the third order method of Cash. Furthermore, it turns out that a Newton-Raphson-Chord method, see [38, 39], is much more efficient (approximately 10–15 % of the computational time) than using a Newton-Raphson method. However, an starting vector estimation for the Newton-Raphson method is always required, see in this context [38].

5 Conclusions

The modeling of electro-thermo-mechanical structures is done on the basis of all possible experimental data, i.e. the temperature-dependent heat capacity, heat conductivity and electrical conductivity as well as the elasticity parameters are obtained and modeled. It turns out that the boundary conditions and the contact conditions between the tools have a significant influence on the accuracy of the prediction, which have to be taken into consideration in future applications. The numerical treatment of the resulting coupled system of differential-algebraic equations is carried out using high-order and time-adaptive schemes. The application of second-order time-integration method using embedded SDIRK-methods yields a sufficient fast computation, particularly, if time-adaptivity is chosen, a starting vector estimation is applied and the Newton-Raphson-Chord method is considered. In this case fast computations are possible even for highly non-linear input data.

Appendix

In the numerical studies the copper is used in the die system. For this the temperature-dependent heat capacity and conductivity are measured, see Fig. 8. The heat capacity at constant pressure of copper is measured with a Netzsch DSC 204 F1 Phoenix apparatus, which uses the Differential Scanning Calorimetry, see Fig. 8b. The thermal diffusivity $a(\Theta)$ of copper is measured with a Netzsch Laserflash LFA 457 and subsequently the thermal conductivity is computed by $\kappa_\Theta(\Theta) = a(\Theta)\rho c_\Theta(\Theta)$, see Fig. 8a. For both quantities a linear temperature dependence is assumed,

$$\kappa_{\Theta,\mathrm{Cu}}(\Theta) = -78.3347 \times 10^{-3} \ \mathrm{W/(mK^2)}\Theta + 433.173\mathrm{W/(mK)} \tag{38}$$

$$c_{\Theta,\mathrm{Cu}}(\Theta) = 82.2141 \times 10^{-3} \ \mathrm{J/(kgK^2)}\Theta + 373.728\mathrm{J/(kgK^2)} \tag{39}$$

which fit very well with experimental data. The properties of alumina and the electrical conductivity of copper are taken from the literature, see [30]. The investigated temperature range in this publication is between 300 K and 1300 K.

$$\kappa_{\Theta,\mathrm{Al}}(\Theta) = \frac{65181330.4 + \Theta}{-669628.8 + 8175.85\Theta} \quad \mathrm{in} \ \ \mathrm{W/(mK)}, \tag{40}$$

$$c_{\Theta,\mathrm{Al}}(\Theta) = \frac{7770.25\Theta}{249.4 + \Theta} + \frac{790.15}{249 + \Theta} + 0.008\Theta \ \ \mathrm{in} \ \ \mathrm{J/(kgK)}, \tag{41}$$

$$\kappa_{\varphi,\mathrm{Al}} = 10^{-8}\mathrm{A/(Vm)} \tag{42}$$

$$\kappa_{\varphi,\mathrm{Cu}}(\Theta) = (5.5 + 0.038\Theta) \times 10^9 \ \ \mathrm{in} \ \ \mathrm{A/(Vm)} \tag{43}$$

References

1. Garay, J.: Current-activated, pressure-assisted densification of materials. Annu. Rev. Mater. Res. **40**(1), 445–468 (2010)
2. Grasso, S., Sakka, Y., Maizza, G.: Electric current activated/assisted sintering (ECAS): a review of patents 1906–2008. Sci. Tech. Adv. Mater. **10**(5), 053001 (2009)
3. Munir, Z.A., Anselmi-Tamburini, U., Ohyanagi, M.: The effect of electric field and pressure on the synthesis and consolidation of materials: a review of the spark plasma sintering method. J. Mater. Sci. **41**(3), 763–777 (2006)
4. Munir, Z.A., Quach, D.V.: Electric current activation of sintering: a review of the pulsed electric current sintering process. J. Am. Ceram. Soc. **94**, 1–19 (2010)
5. Cincotti, A., Locci, A.M., Orru, R., Cao, G.: Modeling of SPS apparatus: temperature, current and strain distribution with no powders. AIChE J. **53**(3), 703–719 (2007)

6. Wang, X., Casolco, S.R., Xu, G., Garay, J.E.: Finite element modeling of electric current-activated sintering: the effect of coupled electrical potential, temperature and stress. Acta Mater. **55**, 3611–3622 (2007)
7. Antou, G., Mathieu, G., Trolliard, G., Maitre, A.: Spark plasma sintering of zirconium carbide and oxycarbide: finite lement modeling of current density, temperature, and stress distributions. J. Mater. Res. **24**, 404–412 (2009)
8. Muñoz, S., Anselmi-Tamburini, U.: Parametric investigation of temperature distribution in field activated sintering apparatus. Int. J. Adv. Manuf, Technol (2012)
9. Wang, C., Cheng, L., Zhao, Z.: FEM analysis of the temperature and stress distribution in spark plasma sintering: modelling and experimental validation. Comput. Mater. Sci. **49**(2), 351–362 (2010)
10. Maizza, G., Grasso, S., Sakka, Y., Noda, T., Ohashi, O.: Relation between microstructure, properties and spark plasma sintering (SPS) parameters of pure ultrafine WC powder. Sci. Tech. Adv. Mater. **8**(7–8), 644–654 (2007)
11. Olevsky, E.A., Garcia-Cardona, C., Bradbury, W.L., Haines, C.D., Martin, D.G., Kapoor, D.: Fundamental aspects of spark plasma sintering: II. Finite element analysis of scalability. J. Am. Ceram. Soc. **95**(8), 2414–2422 (2012)
12. Song, Y., Li, Y., Zhou, Z., Lai, Y., Ye, Y.: A multi-field coupled FEM model for one-step-forming process of spark plasma sintering considering local densification of powder material. J. Mater. Sci. **46**, 5645–5656 (2011)
13. Boley, B.A., Weiner, J.H.: Theory of Thermal Stresses. Dover Publications, Mineola, USA (1997)
14. Nowacki, W.: Thermoelasticity. Addison-Wesley Publishing Co., Reading (1962)
15. Hartmann, S., Rothe, S.: A rigorous application of the method of vertical lines to coupled systems in finite element analysis. In: Ansorge, R., Bijl, H., Meister, A., Sonar, T. (eds.) Recent Developments in the Numerics of Nonlinear Hyperbolic Conservation, Notes on Numerical Fluid Mechanics and Multidisciplinary Design, pp. 161–175. Springer, Berlin (2012)
16. Eringen, A.C., Maugin, G.A.: Electrodynamics of Continua I. Springer, New York (1990)
17. Hairer, E., Wanner, G.: Solving Ordinary Differential Equations II, 2nd revised edn. Springer, Berlin (1996)
18. Strehmel, K., Weiner, R.: Numerik gewöhnlicher Differentialgleichungen. Teubner Verlag, Stuttgart (1995)
19. Krautkrämer, J., Krautkrämer, H.: Ultrasonic Testing of Materials. Springer, Verlag (1990)
20. Workman, G., Kishoni, D., Moore, P.: Ultrasonic testing. Nondestructive testing handbook. American Society for Nondestructive Testing, Nondestructive Testing Handbook (2007)
21. Haupt, P.: Continuum Mechanics and Theory of Materials, 2nd edn. Springer, Berlin (2002)
22. Griffiths, D.J.: Elektrodynamik, 3rd edn. Pearson Education, München (2011)
23. Landau, L.D., Lifshitz, E.M., Pitaevskii, L.P.: Electrodynamics of continuous media, 2nd edn. Elsevier, Amsterdam (2008)
24. Lewis, R.W., Morgan, K., Thomas, H.R., Seetharamu, K.N.: The Finite Element Method in Heat Transfer Analysis. Wiley, Chichester (1996)
25. Quint, K.J., Hartmann, S., Rothe, S., Saba, N., Steinhoff, K.: Experimental validation of high-order time-integration for non-linear heat transfer problems. Comput. Mech. **48**, 81–96 (2011)
26. Reddy, J.N., Gartling, D.K.: The Finite Element Method in Heat Transfer and Fluid Dynamics. CRC Press, Boca Raton, FL (2000)
27. Seifert, W., Ueltzen, M., Müller, E.: One-dimensional modelling of thermoelectric cooling. Phys. Status Solidi **194**(1), 277–290 (2002)
28. Pérez-Aparicio, J.L., Palma, R., Taylor, R.L.: Finite element analysis and material sensitivity of Peltier thermoelectric cells coolers. Int. J. Heat Mass Transf. **55**, 1363–1374 (2012)
29. Palma, R., Pérez-Aparicio, J.L., Taylor, R.L.: Non-linear finite element formulation applied to thermoelectric materials under hyperbolic heat conduction model. Comput. Methods Appl. Mech. Eng. **213–216**, 93–103 (2012)
30. Anselmi-Tamburini, U., Gennari, S., Garay, J.E., Munir, Z.A.: Fundamental investigations on the spark plasma sintering/synthesis process II. Modeling of current and temperature distributions. Mater. Sci. Eng. A **394**, 139–148 (2005)

31. Hairer, E., Norsett, S.P., Wanner, G.: Solving Ordinary Differential Equations I, 2nd revised edn. Springer, Berlin (1993)
32. Ellsiepen, P., Hartmann, S.: Remarks on the interpretation of current non-linear finite-element-analyses as differential-algebraic equations. Int. J. Numer. Methods Eng. **51**, 679–707 (2001)
33. Hartmann, S.: Computation in finite strain viscoelasticity: finite elements based on the interpretation as differential-algebraic equations. Comput. Methods Appl. Mech. Eng. **191**(13–14), 1439–1470 (2002)
34. Hartmann, S., Bier, W.: High-order time integration applied to metal powder plasticity. Int. J. Plast. **24**(1), 17–54 (2008)
35. Hartmann, S., Quint, K.J., Arnold, M.: On plastic incompressibility within time-adaptive finite elements combined with projection techniques. Comput. Methods Appl. Mech. Eng. **198**, 178–193 (2008)
36. Birken, P., Quint, K.J., Hartmann, S., Meister, A.: A time-adaptive fluid-structure interaction method for thermal coupling. Comput. Vis. Sci. **13**, 331–340 (2010)
37. Hamkar, A.-W., Hartmann, S.: Theoretical and numerical aspects in weak-compressible finite strain thermo-elasticity. J. Theoret. Appl. Mech. **50**, 3–22 (2012)
38. Hartmann, S., Duintjer Tebbens, J., Quint, K.J., Meister, A.: Iterative solvers within sequences of large linear systems in non-linear structural mechanics. J. Appl. Math. Mech. (ZAMM) **89**(9), 711–728 (2009)
39. Kelley, C.T.: Solving Nonlinear Equations with Newton's Method. SIAM Society for Industrial and Applied Mathematics, Philadelphia (2003)
40. Bier, W., Dariel, M.P., Frage, N., Hartmann, S., Michailov, O.: Die compaction of copper powder designed for material parameter identification. Int. J. Mech. Sci. **49**, 766–777 (2007)
41. Vanmeensel, K., Laptev, A., Hennicke, J., Vleugels, J., der Biest, O.: Modelling of the temperature distribution during field assisted sintering. Acta Mater. **53**, 4379–4388 (2005)
42. Zavaliangos, A., Zhang, J., Krammer, M., Groza, J.R.: Temperature evolution during field activated sintering. Mater. Sci. Eng. **379**, 218–228 (2004)
43. Ellsiepen, P.: Zeit- und ortsadaptive Verfahren angewandt auf Mehrphasenprobleme poröser Medien. Doctoral thesis, Institute of Mechanics II, University of Stuttgart. Report No. II-3 (1999)
44. Cash, J.R.: Diagonally implicit Runge-Kutta formulae with error estimates. J. Inst. Math. Appl. **24**, 293–301 (1979)